RSC Advances

RSC Advances

www.rsc.org/advances

ROYAL SOCIETY OF CHEMISTRY

www.rsc.org/advances

Table of Contents Graphic
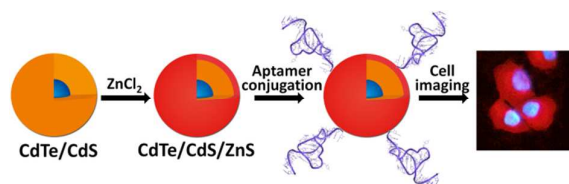
An aqueous approach enhancing the properties of small-core/thick-shell CdTe/CdS nanocrystals by deposition of an outer ZnS shell was developed. The as-prepared nanocrystals were conjugated with aptamer for the targeted imaging of cancer cells.

Journal Name

ARTICLE

One-pot aqueous synthesis of highly strained CdTe/CdS/ZnS nanocrystals and their interactions with cells[†]

Mehriban Ulusoy,[a] Johanna-Gabriela Walter,[a] Antonina Lavrentieva,[a] Imme Kretschmer,[a] Lydia Sandiford,[b] Alix Le Marois,[b] Rebecca Bongartz,[a] Pooyan Aliuos,[c] Klaus Suhling,[b] Frank Stahl,[a] Mark Green,[b*] Thomas Scheper [a*]

In this work, a very simple one-pot synthetic approach was developed to generate aqueous CdTe/CdS/ZnS type-II/type-I red-emitting nanocrystals (NCs). Strain-induced optical properties of CdTe/CdS particles a having core$_{(small)}$/shell$_{(thick)}$ structure with a maximum quantum yield (QY$_{max}$) ~57 % was further improved with the overgrowth of a ZnS shell, resulting in a core$_{(small)}$/shell$_{(thick)}$/shell$_{(small)}$ structure (QY$_{max}$ ~64 %). The spectral properties were tuned further to the near-infrared region as the ZnS shell grew in thickness. X-ray powder diffraction (XRD) analysis and high-resolution transmission electron microscope (HRTEM) images showed the crystalline structure of NCs proving the epitaxial growth of ZnS without crystalline defects. Under continuous UV-irradiation for 5 h, the NCs did not exhibit any photo-degradation but instead displayed a photo-annealing process. These extremely photostable NCs were further characterized in terms of their cytotoxicity and their cell labeling performances. The presence of a ZnS shell was found to reduce the toxicity of the CdTe/CdS NCs. Furthermore, aptamer-conjugated NCs were successfully utilized in targeted cell imaging. Promisingly, the aptamer-NCs bioconjugates were internalized by A549 cells within 2 hours of incubation and retained their fluorescence even after 24 hours of internalization.

Introduction

Core/shell (CS) semiconductor nanocrystals (NCs) emitting in the near-infrared range are of particular interest owing to deep tissue penetration which is important in biomedical imaging applications. Recent studies have mostly concentrated on developing new strategies which allow simple manufacturing of NCs with large spectral shifts. By using the lattice strain between a small soft core (CdTe) and a thick compressive shell (ZnS, CdS, ZnSe, CdSe), Nie and coworkers presented a new class of core$_{(small)}$/shell$_{(thick)}$ NCs displaying type-II behavior with greater photostability and giant spectral shifts in comparison to traditional core$_{(thick)}$/shell$_{(thin)}$ NCs. [1] When the small CdTe core is subjected to a large stress arising from the epitaxial overgrowth of a lattice-mismatched shell, the CdTe core can overcome this stress due to its elasticity while maintaining excellent spectral properties without causing any defect trap sites. The first aqueous synthesis of CdTe/CdS so-called 'magic-core/thick-shell' NIR emitting NCs was reported by Deng and coworkers. [2] They first synthesized magic sized CdTe clusters (~ 0.8 nm), then deposited a thick CdS shell with thickness up to 5 nm creating magic-core/thick-shell NCs with very large spectral shifts and high fluorescence efficiencies. A further study was reported by Chen et al. who used an air-stable Te source (Na$_2$TeO$_3$) instead of NaHTe resulting in a much simpler route to one-pot synthesis of

NIR emitting CdTe$_{(small)}$/CdS$_{(thick)}$ NCs within a reaction time of up to 24 h. [3]

In type-II systems, despite the greater tunability of emission wavelengths and improved fluorescence lifetimes, extended excited-state lifetimes can increase the probability of non-radiative recombination events. One of the separated charge carriers which is confined in the shell region can very likely be trapped in the surface defect sites which further causes the inevitable decrease in fluorescence efficiency. [1] Therefore, the growth of an external shell, resulting in a core/shell/shell (CSS) system, with a wide bandgap serving as an outer protection layer can create more stable NCs while maintaining the lattice strain-induced spectral tuning properties. [4] Taking this into consideration, core$_{(small)}$/shell$_{(thick)}$/shell type-II/type-I CSS NCs can be classified as a new generation of NCs with better optical and structural characteristics. For the fabrication of a CSS structure, zinc sulfide has traditionally been the shell material of choice due to its chemical inertness and negligible toxicity, which attracts specific interest in biological applications. [5, 6] Its wide bandgap energy assures efficient passivation and charge-carrier confinement preventing electron-hole delocalization towards the outer surface, which is hindered by surface traps that reduce fluorescence quantum yields. As a result, a ZnS shell improves chemical stability as well as the optical properties of NCs. [7]

On this basis, a preliminary study was published by Green *et al.* using the aqueous overgrowth of a ZnS shell around CdTe/CdS NCs in 24 h. [8] Very recently, this strategy was further improved by Zhu and coworkers with microwave-assisted irradiation of CdSeTe(small)/CdS(thick) CS NCs and further deposition of a very thin ZnS shell. [9] As a result, QY values were increased by a further ~4 % to 63 % with the overgrowth of a ZnS shell and growth rates were remarkably accelerated in the aqueous phase. However, microwave irradiation is limited in scale-up production and on-line monitoring of the reaction process. Therefore, development of a rapid, facile and user-friendly route to produce high quality water-soluble NCs, especially those of emission wavelengths in the red to near-infrared range, is still highly desirable for the efficient and safe applications of NCs in bio-imaging studies.

Herein, we followed this new generation of magic-core/thick-shell NCs and developed this further for the fabrication of NIR emitting water-dispersed CSS NCs. We have developed a simplified strategy to synthesize core(small)/shell(thick)/shell NCs composed of CdTe/CdS/ZnS based on conventional methods. First, by creating a rich Cd-thiol environment with a very low Te-to-Cd molar ratio, a one-pot aqueous synthesis of type-II CdTe(small)/CdS(thick) with emission wavelengths up to 750 nm (QY$_{max}$ ~ 57 %) was achieved. Afterwards, an outer ZnS shell was grown over the CS NCs by simply injecting a Zn source directly into the crude CS NCs solution. After 3 h of reaction, high quality CdTe(small)/CdS(thick)/ZnS(thin) CSS NCs emitting in the red-to-near infrared window were obtained with improved fluorescence efficiency (QY$_{max}$ ~ 64 %). As a result, the one-pot synthesis of highly tunable NIR emitting type-II/type-I CdTe/CdS/ZnS CSS NCs with a very narrow FWHM (full width at half maximum) values (max. 80 nm) and high quantum yields was performed without precursor injection and purification steps.

These improved optical properties allowed us to successfully implement these NCs in targeted cell imaging after conjugation with S15 DNA aptamers which specifically bound to lung cancer cells. [10] Aptamers are short, single-stranded oligonucleotides generated from an *in vitro* process known as SELEX (Systematic Evolution of Ligands by Exponential enrichment). [11] Their high binding affinity and selectivity towards numerous targets, including small molecules, proteins, receptors, and cells in addition to their chemical stability, economic production and convenient modification introduced aptamers as a novel type of recognition molecules. [10] There are various successful reports presenting the efficiency of aptamer conjugated nanoparticles for sensing, [7, 12-15] imaging and therapeutic applications. [16-19] Fluorescence microscopy studies showed the effective up-take of aptamer-NCs bioconjugates by A549 lung cancer cells.

Results and Discussion

Production and optical analysis of NCs

For the one-pot synthesis of CdTe(small)/CdS(thick) NCs, a Cd-rich environment was created by using a very low Te-to-Cd (1:25) molar ratio. 3-mercaptopropionic acid (MPA) was utilized as a sulphur source as well as the surface functionalization agent. At the early stage of particle growth, the usage of a very low Te-to-Cd molar ratio resulted in the formation of a small population of small particles. [20] In this case, depletion of free monomers proceeded slower than in the case of higher Te-to-Cd ratios. The extended depletion time of monomers avoided the Oswald ripening process, a process which originated from a slow-growth rate, resulting in a broadening of size distributions. [21] At this early stage of crystal growth, the monomer concentrations should be rather high and addition of monomers to the crystals should be predominant for the growth of particles. In this case, diffusion controlled growth via monomer addition facilitates faster growth of smaller particles than the larger ones. Moreover, Cd precursors which are improved by high pH and Te precursor stability support this fast growth process. [22] In regards to the effect of ligand-to-Cd ratio on the growth rate of NCs, the ligand-to-Cd molar ratios lower than 2:1 create an environment dominant with monothiol complexes rather than dithiol complexes. Under high pH conditions (> 11), these monothiol complexes have greater solubility which improves the release of Cd and therefore support formation of CdTe monomers for nucleation and particle growth. Thus, a fast growth rate is achieved by means of accelerated Cd release for crystal growth under low ligand-to-Cd molar rations and high pH conditions. [22] Once the Te source is depleted, the remaining Cd-monothiol complexes give a Cd rich surface which supports CdS shell formation around those very small CdTe particles resulting in core(small)/shell(thick) CdTe/CdS nanocrystals. This mechanism explains the high quality optical characteristics obtained by one-pot formation of core/shell (CS) structures.

Absorbance and fluorescence spectra of the resulting CdTe/CdS NCs, shown in Fig. 1a-b, reveal the gradual spectral shift to the longer wavelength as the CdS shell proceeded to grow in thickness. Notably, samples did not show a sharp first exciton absorption peak but a featureless profile with the increase of particle size. This complete disappearance of the first exciton absorption peak can be attributed to transition of type-I to type-II behaviour. [1] During this switch, gradual strain-induced spectral changes did not exhibit abrupt transformations allowing the preservation of tunability of emission spectra by lattice strain. The soft CdTe core was able to compress elastically as the CdS shell grew in thickness causing a large stress to the core. This elasticity of the very small CdTe core material allowed these NCs to maintain and even improve their optical properties. CdTe/CdS NCs emitting at 730 nm were obtained after 6 h of synthesis at 90 °C. Quantum yields (QY %) reached a maximum value of 57 % when the emission wavelength shifted to around 650-660 nm which was followed by a decrease as the CdS shell proceeded to grow further (Fig. 1e). It is likely that the CdTe core could no longer withstand the strain without forming surface traps.

Interestingly, when a ZnS shell material with a larger lattice-mismatch was overgrown on the surface, the QY started to increase again but only until a certain shell thickness. When the ZnS shell was deposited around CdTe/CdS NCs having a QY$_{max}$ ~57 % ($\lambda_{emission}$= 650-660 nm), the resulting CSS NCs exhibited improved fluorescence behaviour with a QY$_{max}$ ~ 64 % (Fig. 1e, left-inset). Later, another CS NCs having a reduced QY ~53 % ($\lambda_{emission}$= 672 nm) was used for the ZnS shell formation. Again, the fluorescence efficiency of the resulting CSS NCs was improved further to a QY$_{max}$ ~ 57 % (Fig. 1e, right-inset). To the best of our knowledge, the obtained optical yields for the water-dispersed red-emitting CdTe/CdS/ZnS NCs are one of the highest values in comparison to the literature values (Table 1). These results indicated that epitaxial growth of a ZnS shell around a CdS shell improved the surface structure of NCs by passivating the dangling bonds on the surface. However, we should note that the big lattice mismatch (16.4 %) between CdTe and ZnS did not allow us to grow a thick epitaxial ZnS shell without crystalline defects. After a very thin ZnS formation, NCs could not maintain their excellent fluorescence efficiencies causing reduced QY values. It is remarkable that highly strained CdTe/CdS/ZnS CSS heterostructures exhibit excellent photoluminescence properties especially when it is considered that crystallinity of the core and the homogeneity of shells were achieved at very low temperatures under atmospheric conditions. Another promising feature of the external ZnS shell growth is the gradual

tuning of the emission spectra to longer wavelengths without formation of any deep-trap emission (Fig. 1c-d). After 6 h of reaction, emission wavelengths were shifted aproximately 16-19 nm to the near-infrared region. As expected from the type-I behaviour of the CdS/ZnS shell/shell heterostructure, the spectral shifts are not as large as in type-II behaving CdTe/CdS core/shell NCs. Moreover, utilization of MPA as a sulphur source for the ZnS shell formation which is already present in the crude CdTe/CdS solution, created more controllable and reproducable shell formation with reduced growth rates in comparison to sodium sulfide (Na_2S). Sodium sulfide has relatively high decomposition rate causing uncontrolled release of sulphur ions and thus a fast growth rate. [21] Hovever, deposition of an even ZnS shell required a slow growth step. [8]
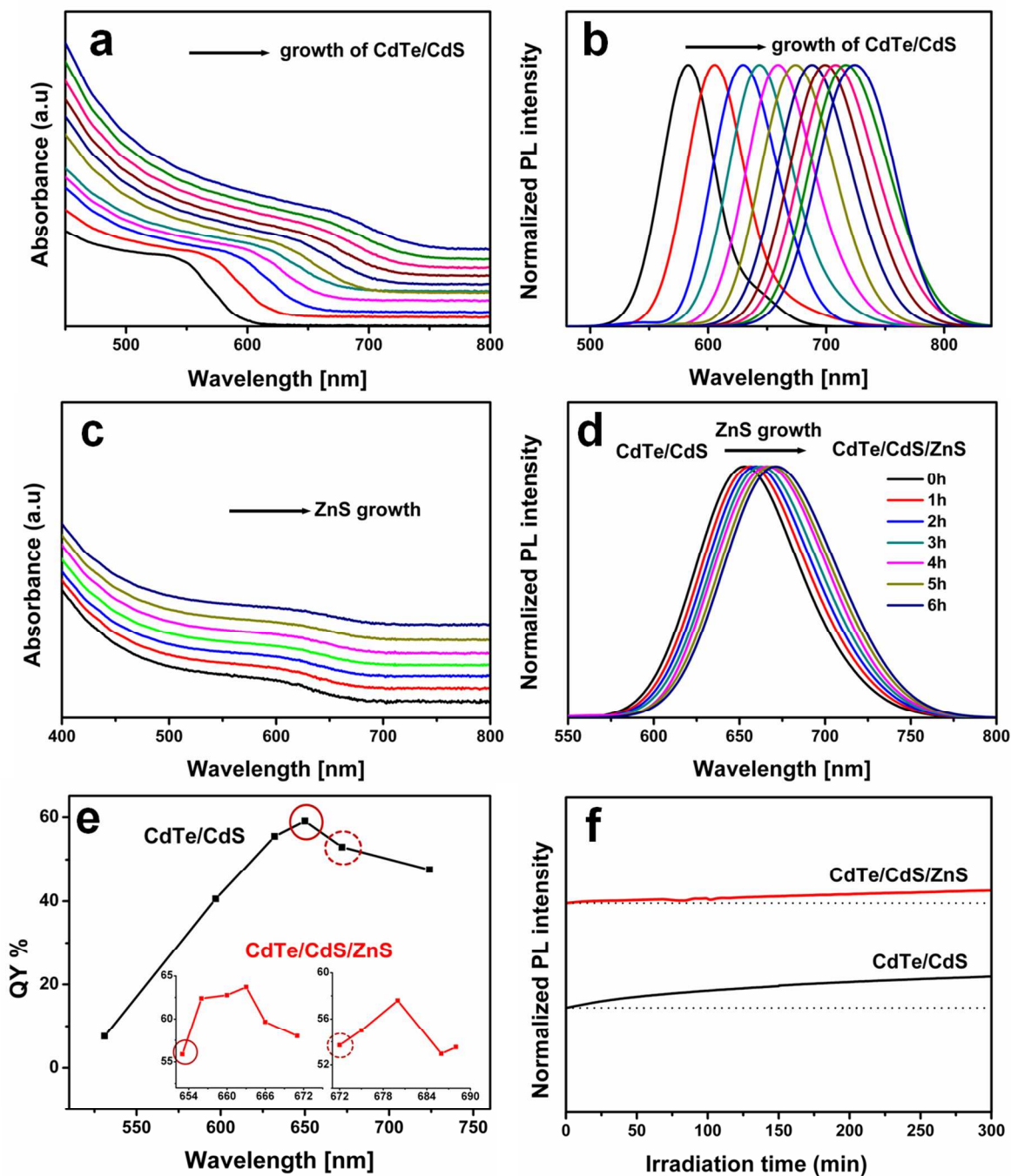

Figure 1. Optical characteristics of NCs. Absorbance (a) and fluorescence emission spectra of CdTe/CdS CS NCs during particle growth for 6 h (b). Absorbance (c) and fluorescence emission profiles of CdTe/CdS/ZnS CSS NCs during ZnS shell growth for 6 h ($\lambda_{excitation}$= 470 nm) (d). Fluorescence efficiencies of CS and CSS NCs in terms of quantum yields (QY %) (e). Right insert shows the QY % of CSS NCs deposited on CS NCs ($\lambda_{emission}$= 672 nm). Left inset shows the QY % of CSS NCs deposited on CS NCs ($\lambda_{emission}$= 652 nm). Photostability of CS NCs and corresponding CSS NCs during continuous irradiation under UV light at 360 nm for 5 h (f).

Table 1. Comparison of optical properties of core/shell/shell NCs synthesized with aqueous approaches

Core/shell/shell structure	Emission	QY_{max} %	Synthetic route	Reference
$CdTe_{(large)}/CdS_{(thin)}/ZnS_{(thin)}$	615 nm	43	microwave (step-wise)	He et al., 2008 [23]
$CdTe_{(large)}/CdS_{(thick)}/ZnS_{(thin)}$	660 nm	n.d *	conventional (one-pot)	Green et al., 2009 [8]
$CdTe_{(large)}/CdS_{(thin)}/ZnS_{(thin)}$	615 nm	45	autoclave/conventional	Tian et al., 2010 [24]
$CdTe_{(large)}/CdS_{(thin)}/ZnS_{(thin)}$	625 nm	42	conventional (step-wise)	Li et al., 2011 [25]
$CdTe_{(large)}/CdSe_{(thin)}/ZnSe_{(thin)}$	670 nm	<5	conventional (one-pot)	Green et al., 2011 [26]
$CdTe_{(large)}/CdS_{(thin)}/ZnS_{(thin)}$	613 nm	15	conventional (one-pot)	Zhang et al., 2012 [27]
$CdSeTe_{(small)}/CdS_{(thick)}/ZnS_{(thin)}$	648 nm	63	microwave/conventional	Li et al., 2013 [9]
$CdTe_{(small)}/CdS_{(thick)}/ZnS_{(thin)}$	650-660 nm	64	conventional (one-pot)	present study

* not determined

Structural Analysis of NCs

Diffraction patterns of CS-I (CdTe/CdS, $\lambda_{emission}$=550 nm), CS-II (CdTe/CdS, $\lambda_{emission}$=655 nm) and its corresponding CSS-I (CdTe/CdS/ZnS, $\lambda_{emission}$=668 nm) and CSS-II (CdTe/CdS/ZnS, $\lambda_{emission}$=687 nm) NCs revealed that these nanoparticles had a zinc blende cubic crystal structure (Fig. 2). For the CS NCs, as the CdS shell grew in thickness, diffraction angles shifted to higher values towards the position of standard CdS diffraction angles. As an outer ZnS shell was grown over CS-II, a further shift of the diffraction peaks to higher angles was observed whilst maintaining the pattern of the cubic lattice. The peak widths and shapes of CSS-I and CSS-II NCs remained nearly unchanged in comparison to those of the CS nanocrystals, which confirmed the formation of a core/shell/shell structure rather than an alloyed structure. A homogeneous alloy would result in a significant narrowing of XRD peak widths upon increasing particle size. [23]
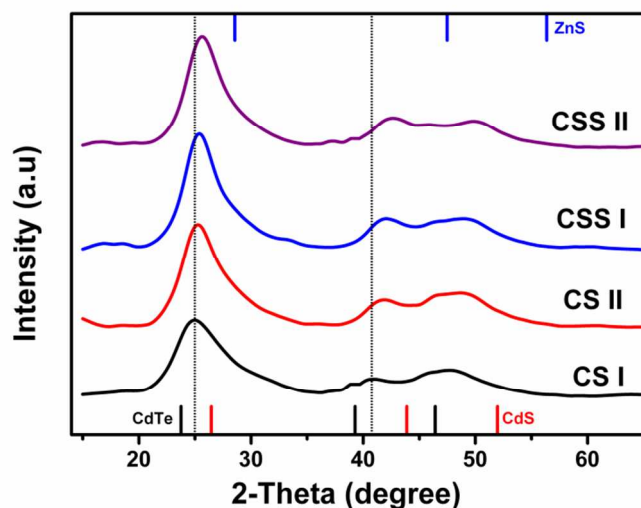

Figure 2. Diffraction patterns of CS- I (CdTe/CdS, $\lambda_{emission}$=550 nm), CS- II (CdTe/CdS, $\lambda_{emission}$=655 nm) and its corresponding CSS-I (CdTe/CdS/ZnS, $\lambda_{emission}$=668 nm) and CSS-II (CdTe/CdS/ZnS, $\lambda_{emission}$=687 nm). The standard diffraction pattern of the reference cubic structures of CdTe (lattice constant a= 6.4827 Å), CdS (a=5.8304 Å) and ZnS (a= 5.4109 Å) is also shown.

High-resolution transmission electron microscopy (HRTEM) was used to further investigate the morphology and crystal structure of the NCs. Fig. 3 (a-d) show low and high magnification TEM images of the as-prepared CdTe/CdS CS NCs, indicating these nanocrystals have either spherical or tetrahedral structures with an average size of 3.68 ± 0.74 nm. HRTEM images of different typical

tetrahedral NCs are displayed in Fig S1. The mean crystalline diameter of CdTe/CdS was further confirmed from the line width of the XRD spectrum using Scherrer's formula; d= 0.94 $\lambda/(B \cos\theta_B)$, where λ is the X-ray wavelength (Cu $_{K}\alpha$ = 1.54 Å), B is the full width at the half maximum of the diffraction peak (radians), and θ_B is the half angle of the (111) diffraction peak on the 2θ scale. [27] It was calculated to be 3.35 nm which is consistent with TEM size analysis proving NCs have an almost single crystalline structure. HRTEM images of CdTe/CdS/ZnS NCs in Fig. 3 (e-f) and the indexed fast-Fourier transformation (FFT) feature further confirmed the crystallinity of the NCs with the existence of well-resolved lattice planes. The lattices stretch straight across entire nanocrystals demonstrating coherent epitaxial growth of shell material without forming crystalline defects. Further, atomic force microscopy (AFM) images of CdTe/CdS/ZnS NCs are depicted in Fig S2 showing a topographical view of single nanocrystals. From the TEM images, the average size of CdTe/CdS/ZnS NCs was calculated to be 4.31 ±0.76 nm. ZnS shell thickness was determined to be 0.31 nm which corresponds to ~1.1 monolayers (ML), assuming a monolayer of cubic ZnS is 2.705 Å (half the cell unit). Resulting NCs will be presented in the following text as CSS (1.0 ML).

The as-prepared CdTe/CdS and CdTe/CdS/ZnS NCs showed an average d-spacing [111] of 0.344 nm and 0.351 nm, respectively, which appeared inbetween the standard interplanar distances of cubic CdTe (0.374 nm) and CdS (0.336 nm). The lattice distances of [111] planes were also estimated by using the Bragg formula of X-ray diffraction which is d= $n\lambda/(2 \sin\theta_B)$, where λ is the X-ray wavelength (Cu $_{K}\alpha$ = 1.54 Å), n is an integer, and θ_B is the half scattering angle of the (111) diffraction peak on the 2θ scale. It was found to be 0.353 nm for CdTe/CdS and 0.351 nm for CdTe/CdS/ZnS, which are in good agreement with the lattice spacing values obtained from HRTEM images. These obtained d-spacing values of highly-strained CdTe/CdS/ZnS NCs being shifted towards to lattice spacing of standard cubic CdS reveals that CSS NCs mostly maintain the structural details of the CdS shell. These results are quite expected when it is considered that the compressive behavior of a CdS shell means it will adopt its bulk lattice parameters once it reaches a thickness large enough to compress the CdTe core. [1] Moreover, the thin ZnS shell (1.0 ML) at the surface adopted the lattice constant of the CdS inner shell and therefore did not exhibit any observable effect on the lattice spacing values of the as-prepared CSS NCs.

Furthermore, time-resolved fluorescence decay curves of CSS NCs were analyzed in order to measure excited-state lifetimes of the as-prepared NCs (Fig. S3). Fluorescence decay curves were fitted by tri-exponential model using the Levenberg-Marquardt algorithm. The fit parameters are listed in Table S1. As a result, CSS NCs feature an average lifetime of 51.7 ns, consistent with a typical type-II structure. [2, 9]
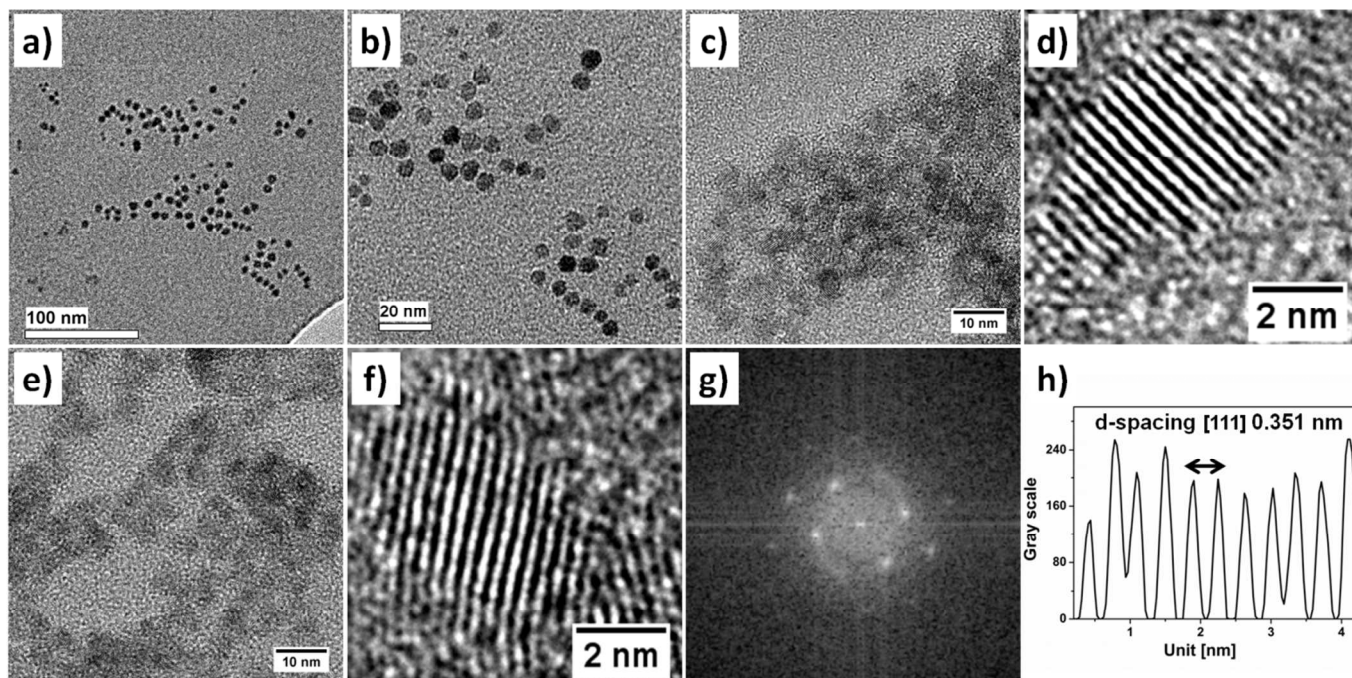
Figure 3. TEM images of CdTe/CdS NCs with low (a) and high magnifications (b), HRTEM images of CdTe/CdS NCs with a low (c) and a high magnification (d), HRTEM images of CdTe/CdS/ZnS NCs with a low (e) and a high magnification (f), a corresponding fast- Fourier transformation (FFT) profile of CdTe/CdS/ZnS NCs (g) and plotted profile of lattice plane distances along the CdTe/CdS/ZnS lattice lines (h).

Photostability

Photostability studies of CdTe/CdS and corresponding CdTe/CdS/ZnS revealed that both NCs were extremely stable under continuous UV-irradiation for 5 h (Fig. 1f). During the irradiation, the fluorescence intensity of CdTe/CdS increased by ~30 % of the initial signal whilst the fluorescence intensity of CdTe/CdS/ZnS showed only a ~12 % increase. After the irradiation, the emission profiles of the NCs were measured and no significant spectral shifts to the blue region were observed which eliminates the possibility of photo-oxidation (Fig. S4). This increase in fluorescence intensity under irradiation phenomenon can be either attributed to photo-brightening or photo-annealing processes. Photo-annealing is caused by the structural rearrangements at the core-shell interfaces as well as at the surface and, is therefore permanent. On the other hand, photo-brightening effects vanish once the excitation source is removed, thereby being only temporary. [28] Since the fluorescence enhancement was permanent when the UV light was removed, we can assume that the photo-annealing effect is the most likely reason for the increase. Moreover, the photo-annealing effect under irradiation can be more pronounced for the NCs with a higher concentration of surface defects at the particle surface. [12] This reasonably explains the predominant enhancement in fluorescence intensity of CdTe/CdS NCs.

Cytotoxicity

For biomedical applications, the toxicity of Cd-based NCs is a critical point of discussion because of their heavy metal (Cd^{2+}, Te^{2-}) containing composition. [29] Therefore, *in vitro* cellular toxicity of NCs must be studied prior to *in vivo* application. In this study, *in vitro* cytotoxicity effects of developed NCs on A549 adenocarcinoma lung cancer cells was studied by treating the cells with different concentrations (0.002-600 µg/ml) of NCs composed of different sizes, shell compositions and shell thicknesses. First, cells were exposed to CS 550 and CS 659 (CdTe/CdS emitting at 550 nm and 659 nm, respectively) to investigate the NC size effect on cellular toxicity. In the next step, a ZnS shell (0.5 ML) was deposited on CS 659 NCs to evaluate the effect of outer shell composition. In the final step, a thicker ZnS shell (1.0 ML) was overgrown around CS NCs to compare the impact of ZnS shell thickness on the toxic effects of NCs. Cell viability obtained from a CellTiter-Blue assay showed that cells retained more than 70 % of their viability when they were exposed to high concentrations of NCs for 2 h (Fig. 4a). Since ≤ 30 % reduction in cell viability is the accepted limit for the biocompatibility of the tested material according to ISO 10993-5.2009 cytotoxicity standards, it can be assumed that NCs didn't generate significant toxicity after 2 h of exposure time. When the exposure time was prolonged to 24 h, high concentrations of NCs induced toxicity at different levels with a correlation to the particle size, shell composition and ZnS shell thickness. IC_{50} values (half-maximal inhibitory concentration, i.e. the dose applied by which 50 % of cells died) demonstrate that smaller CS NCs caused more toxicity (IC_{50} 83 µg/ml) in comparison to their larger CS counterparts (IC_{50} 99.9 µg/ml). When a ZnS (0.5 ML) shell was overgrown around the CS NCs, the resulting CSS NCs exhibited significantly reduced cellular toxicity when compared to their CS NCs counterpart. As ZnS shells grew in thickness (1.0 ML), the IC_{50} value was increased further from 116.6 to 150.8 µg/ml.

The main cause of cellular toxicity of Cd-containing NCs has been mostly attributed to the release of Cd^{2+} ions to the intracellular environment after particle internalization. The internalized NCs

likely underwent a degradation process followed by a loss of their surface coating molecules and later the release of their metal ions via surface etching processes. Moreover, NCs with sizes less than 10 nm,
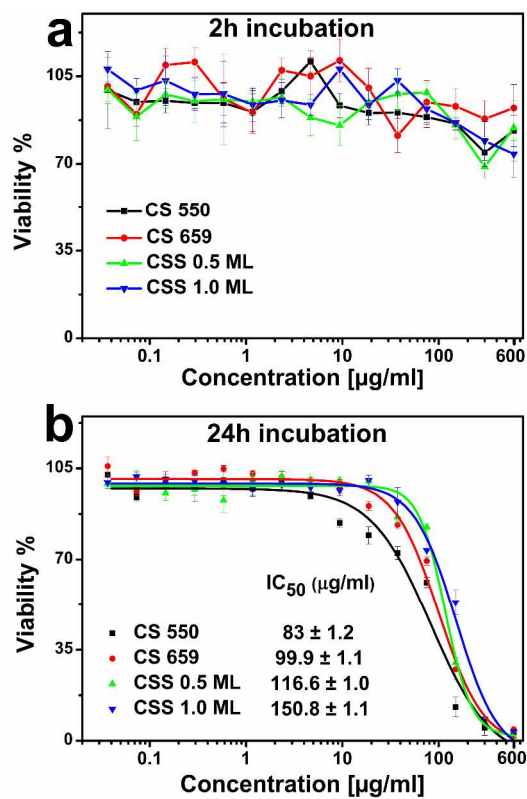

Figure 4. Viability of A549 adenocarcinoma lung cancer cells treated with CS 550 (CdTe/CdS, $\lambda_{emission}$=550 nm), CS 659 (CdTe/CdS, $\lambda_{emission}$=659 nm) and its corresponding CSS 0.5 ML (CdTe/CdS/ZnS, 0.5 ML ZnS) and CSS 1 ML (CdTe/CdS/ZnS, 1 ML ZnS) with a concentration range 0.002-600 µg/ml. CellTiter-Blue assay was performed with the cells incubated with with NCs for 2 h (a) and 24 h (b). Half-maximal inhibitory concentration (IC_{50}) values were calculated by fitted dose-response curves (presented data as mean±standard deviation of 4 replicates).

which have high surface area to volume ratios, induce more pronounced cellular damage in comparison to larger NCs. [30, 31] In general, the toxicity decreases with increasing particle sizes. [32] Regarding the size-dependent cytotoxicity of NCs, we confirmed the pronounced toxicity of smaller NCs in comparison to larger ones with the same core/shell composition as well as similar surface structure. On the other hand, the presence of a well-passivating protective ZnS shell layer can likely minimize the destabilization of NCs to a large extent and therefore prevent the release of highly toxic metal ions. [23, 33] The obtained cell viability results of CSS NCs meet the expectations of the inert nature of ZnS, building a strong electronic barrier at the NCs surface and therefore resulting in reduced cytotoxic effects.

Cell imaging with aptamer conjugated NCs

CdTe/CdS/ZnS NCs modified with aptamers were tested for their targeted *in vitro* cell imaging applicability. We first conjugated the carboxyl terminated CdTe/CdS/ZnS NCs to amine-terminated S15 DNA aptamers which target adenocarcinoma lung cancer cells (dissociation constant, K_d 56.8 nM) [10] using EDC coupling

chemistry (S15-NCs). As a negative control, bare NCs and NCs conjugated with a random oligonucleotide (Oligo-NCs) were applied to the A549 cells using the same experimental conditions. Migration behaviors of NC conjugates were analyzed with agarose gel electrophoresis (Fig. S5). As predicted, NCs conjugated to aptamer or oligonucleotide migrated slower in comparison to bare NCs. However S15/NCs and Oligo/NCs exhibited similar migration pattern despite of different molecular weights. We attribute this effect to the reduced sizes of oligonucleotides in their three-dimensional structures which are rather indistinguishable in terms of their electrophoretic mobility.

Fluorescence microscopy images illustrated in Fig. 5, reveal the internalization of S15-NCs in the lung cancer cells within 2 h of incubation (Fig. 5a). At the same time, Oligo-NCs as well as bare NCs did not accumulate in the cells within the given incubation time (Fig. 5c-d). Promisingly, aptamer-NC conjugates were still observable under the microscope after 24 h of internalization, indicating the long-term stability of developed NCs inside the cells (Fig. 5b). Accordingly, we can draw the conclusion that S15 DNA aptamers are efficient as a targeting moiety against lung cancer cells and in combination with the excellent optical properties of the NCs, present a novel platform for the application of developed NCs for targeted cell imaging studies.
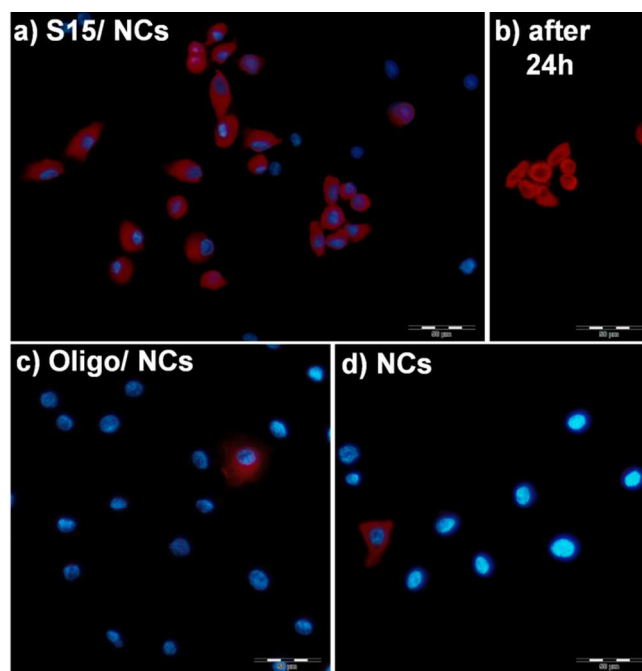

Figure 5. Fluorescence microscope images of A549 adenocarninoma lung cancer cells treated with S15 aptamer-NCs conjugates (a), oligo-NCs (c), and bare NCs (d) for 2 h. Images of cells treated with S15-NCs after 24 h of internalization (b). Cell nuclei were counterstained with DAPI. Scale bar 50 µm.

Experimental

Materials

$CdCl_2.2^{1/2}$ H_2O (cadmium chloride (pentahydrate), 98 %>), Na_2TeO_3 (sodium tellurite, 99.5 %), $ZnCl_2$ (zinc chloride, anhydrous, 99.99 %), 3-mercaptopropionic acid (MPA, 99 %), $NaBH_4$ (sodium borohydride, > 98.0 %), trisodium citrate dehydrate, N-(3-dimethylaminopropyl)-N'-ethylcarbodiimide hydrochloride (EDC), boric acid and rhodamine 6G (dye content ~95 %) were purchased

from Sigma-Aldrich GmbH, Munich. Qdot® 655 ITK™ carboxyl quantum dots (QY 87 %) were obtained from Life Technologies GmbH, Darmstadt. CellTiter-Blue cell viability assay reagent was purchased from Promega GmbH, Mannheim. S15-amino(C6) aptamer and control DNA-amino(C6) were purchased from BioSpring GmbH, Frankfurt. All chemicals were used as they were received without any purification. All solutions were prepared with distilled water if not indicated otherwise.

Sequence of 5'- amino(C6)-S15 DNA aptamer:

5'ACGCTCGGATGCCACTACAGGCTATCTTATGGAAATTTC GTGTAGGGTTTGGTGTGGCGGGGCTACTCATGGACGTGCT GGTGAC3'[10]

Sequence of random 5'- amino(C6)-oligonucleotide:

5'ATACGGGAGCCAACACCAGCAGTCAAGAAGTTAAGAGA AAAACAATTGTGTATAAGAGCAGGTGTGACGGAT3'

For cell culture experiments, Dulbecco's Modified Eagle Medium (DMEM, Sigma- Aldrich GmbH, Munich) supplemented with 10 % (v/v) fetal calf serum (FCS, Biochrom GmbH, Germany) and 1 % (v/v) penicillin/streptomycin (P/S, Biochrom GmbH, Germany) was used as cell culture medium. For fluorescence imaging experiments, cells were seeded on LabTek® II glass chamber slide systems with CC2 treatment (Nalge Nunc International, USA).

Buffers

Aptamer selection buffer (pH 7.4) was prepared with 2.67 mM calcium chloride, 1.47 mM calcium dihydrogen phosphate, 137.93 mM sodium chloride, 8.06 mM disodium hydrogen phosphate, 5 mM magnesium chloride, 4.5 g/L glucose and 1 mg/ml bovine serum albumin (Sigma- Aldrich GmbH, Munich). Incubation buffer was prepared from the selection buffer by addition of 2 % (v/v) FCS. Phosphate buffered saline (PBS) was prepared with 137 mM sodium chloride, 2.7 mM calcium chloride, 10.1 mM disodium hydrogen phosphate and 1.8 mM calcium dihydrogen phosphate. Solution pH was adjusted to 7.4 and then sterilized.

Synthesis of CdTe/CdS

$CdCl_2$ (125 mM, 1 ml), 18.5 µl 3-mercaptopropionic acid (MPA), trisodium citrate dehydrate (42.5 mM, 1 ml), sodium tellurite (5 mM, 1 ml) and sodium borohydride (125 mM, 1 ml) were added sequentially into a three-neck round bottom flask. 21 ml ddH_2O was added to give a final volume of 25 ml. The molar ratio of Cd/Te/MPA was set to be 1/0.04/1.7. Under mixing, the solution pH was adjusted to 11.4 with 1 M NaOH. Reaction solution was then heated to 90 ^{o}C at a heating rate of approximately 3.5 ^{o}C/min. The solution was then refluxed with an air condenser (Findenser, Radleys, UK) eliminating the necessity of any tubing systems for water cooling making the procedure simpler and more economic. Once the reaction solution reached a temperature of 90 ^{o}C, the samples were collected at different time intervals during 6 h. Absorbance and fluorescence measurements were made with crude samples after cooling to room temperature. For storage, samples were precipitated with 2-propanol and collected via centrifugation. The precipitate was weighted after it was dried. Later, it was re-dissolved in water and stored at 4°C.

Deposition of ZnS shell

The as-prepared CdTe/CdS solution ($\lambda_{emission}$= 650-660 nm, QY ~ 57 %) was directly used for the external synthesis of ZnS. 12 ml of the CdTe/CdS crude solution, 12 ml ddH_2O and 1 ml $ZnCl_2$ solution (25 mM) was stirred giving a final volume of 25 ml. The final pH of the reaction solution was adjusted to 11.5 with 1 M NaOH. Then, the solution was heated slowly to 65 ^{o}C and the ZnS shell growth was monitored for 6 h. Apart from dilution, no post-synthesis treatment was made for any of the samples before absorbance and fluorescence measurements. For cell culture experiments, samples were precipitated with 2-propanol and collected via centrifugation. The colloidal precipitate was weighed after drying and re-dissolved in water. Later, this was washed with ddH_2O using 10 kDa MWCO membrane filters (PES, Vivaspin, Sartorius Stedim Biotech GmbH, Germany) and stored at 4°C.

Measurement of QY %

Fluorescence quantum yields (QY %) were determined by using commercially available Qdot® 655 ITK™ carboxyl quantum dots (QY 87 %) as a reference. Rhodamine 6G was used first as a cross-reference to confirm the QY % of the commercial Qdot655 and it was found to be 86.7 ± 0.5 % which is consistent with the QY value given by the manufacturer. Then, the as-prepared colloidal samples as well as the reference solution were diluted to give an equal absorbance below 0.1 at the excitation wavelength (470 nm). The integrated area of corresponding emission curves were analyzed and compared with the integrated area of emission curve of reference Qdot655 sample in the same solvent (Equation 1).

$$QY \%_{(sample)} = QY \%_{(reference)} \frac{Area_{(sample)}/Area_{(reference)}}{Abs_{(reference)}/Abs_{(sample)}} \quad (1)$$

Photostability study

To exclude the effect of residual reagents, purified CdTe/CdS and CdTe/CdS/ZnS samples were tested for their photostability. 1 ml of diluted samples were irradiated with UV light (360 nm) continuously for 5 h by using 150-W xenon lamp. The corresponding fluorescence intensity was recorded every 10 s.

Structural analysis

X-ray diffraction patterns of CdTe/CdS NCs and corresponding CdTe/CdS/ZnS NCs were analyzed with a Bruker D8 Advance diffractometer using Cu Kα radiation (λ = 1.5418 Å). For the measurements, samples were precipitated with 2-propanol after synthesis and dried under vacuum to yield powdered samples, which were deposited on a single-crystal Si wafer. Transmission electron microscopy (TEM) and high-resolution transmission electron microscopy (HRTEM) measurements were conducted with FEI Tecnai T20 (FEI, USA) and FEI Tecnai G2 F20 TMP-TEM with a 200 kV FEG (field emission gun) in bright field mode, respectively. Samples were prepared from solution by placing a droplet on a carbon coated mesh copper grid and drying in air. Topographic images of CdTe/CdS/ZnS NCs were taken with Nanowizard II atomic force microscope (AFM) from JPK-Instruments AG (Berlin, Germany). Images of 2µm- 2µm size were collected at a 0.5 Hz scan rate and 1024x1024 pixel resolutions. In order to reach high resolution, a very sharp AFM cantilever of MSNL (nominal tip radius approx. 2 nm, nominal force constant 0.6 N/m) from Brucker Corporation (CA, USA) was used. A drop of 50 µl of diluted NCs suspension was placed onto a clean polysine microscope adhesion

slide (Thermo Fisher Scientific Inc. USA) and was allowed to dry at room temperature. The glass slide was then mounted onto an inverted light microscope (AxioObserver D1, Zeiss AG, Jena, Germany). Thereafter, the AFM was placed on the light microscope and imaging was employed in air using contact mode. Fluorescence decay curves were collected by a HPM 100-40 detector (Becker&Hickl GmbH, Germany), and time-correlated single photon-counting (TCSPC) was achieved by a SPC-150 module (Becker&Hickl GmbH, Germany). 10μL of the NC suspension was placed on the stage of a Leica TC SP2 inverted scanning confocal microscope with a water 1.2NA 63x objective. The sample was excited by a picosecond pulsed diode laser (Hamamatsu Photonics, Japan) at 467 nm with a repetition rate of 1MHz.

Cytotoxicity study

For the cytotoxicity studies, human lung adenocarcinoma A549 cells (ACC107) purchased from DSMZ (German Collection of Microorganism and Cell Cultures) were used with a passage number of less than 20. CellTiter-Blue (CTB) cell viability assay was performed for an indirect estimation of the numbers of viable cells to evaluate the cytotoxicity of CdTe/CdS and CdTe/CdS/ZnS NCs. It uses the indicator dye resazurin which is reduced by viable cells into highly fluorescent resorufin ($579_{Ex}/584_{Em}$). The procedure was performed as follows: A549 cells (8000 cells/well) in culture medium (DMEM supplemented with 10 % FCS and 1% P/S) were cultured in 96-well plates (100 μl/well) and incubated for 2 days at 37 °C, 5 % CO_2, > 90° humidity. NC dilution series were prepared with cell culture medium, and 100 μl of NC solutions were added to each well. A549 cells were treated with NCs for 2 h and 24 h. After incubation, cells were washed gently with PBS buffer 2 times. CTB reagent was diluted 1:6 with DMEM medium (without supplement), and 100 μl of mixture was added to each well and incubated for 2 h (37 °C, 5% CO_2). Finally, the resulting fluorescence intensities were recorded, and cell viability was calculated using the fluorescence intensity of untreated cells as a reference. Dose-dependent response curves were evaluated by fitting the concentration-dependent experimental cell viability data with dose-response non-linear fitting function (Origin Pro 8.5, Origin Lab Corp. USA). Half-maximal inhibitory concentrations (IC_{50}) were calculated from the fitted dose-response curves.

Conjugation with Aptamer

CdTe/CdS/ZnS NCs ($\lambda_{emission}$= 668-670 nm) were labeled with S15-Amino aptamers for targeting of A549 lung adenocarcinoma cells through EDC coupling reaction between carboxyl groups of NCs and amino groups of aptamer molecules. S15-Amino aptamer (177 μM, 16 μl) solution was added to CdTe/CdS/ZnS (9 mg/ml, 24.4 μl) solution dissolved in sodium borate buffer (10 mM, pH 7.4) to give a final volume of 100 μl, and mixed for 5 min at room temperature. Then, 10 mg/ml EDC solution (6.5 μl) dissolved in sodium borate buffer (10 mM, pH 7.4) was added to the mixture and incubated for 3 h at room temperature. After coupling, S15-NCs conjugates were purified with centrifugation through membrane filters (50 kDa MWCO PES, Vivaspin, Sartorius Stedim Biotech GmbH, Germany). The purification step was repeated 8-9 times with 50 mM sodium borate buffer (pH 8.3). As a negative control, CdTe/CdS/ZnS NCs were conjugated with a random oligonucleotide (Oligo-NCs) using the same procedure. 20 μl of NCs conjugates were applied to agarose gel electrophoresis. 1.5 % agarose gel was run at 100V for 10 min and then viewed with a gel imaging system equipped with an UV transilluminator (INTAS Science Imaging Instruments GmbH, Germany) after 0.40 seconds of exposure time.

Cell imaging

A549 cells were treated with unconjugated and aptamer-conjugated CdTe/CdS/ZnS NCs. NC conjugates were first transferred to binding buffer prior to treatment. A549 cells in cell culture medium were seeded on glass chamber slides (Nunc LabTek-II with CC2 treatment) and allowed to grow for 2 days at 37 °C, 5 % CO_2. After cell culture medium was removed, cells were treated for 15 min with incubation buffer (selection buffer with 2 % FCS). Incubation buffer was then removed and cells were treated with 200 μl of bare NCs (0.125 mg/ml), S15-NC (0.125 mg/ml) and Oligo-NC conjugate solutions (0.125 mg/ml) which were diluted in incubation buffer. A549 cells were then incubated with the conjugates for 2 h. After that, incubation buffer was removed and cells were washed gently with warm PBS solution 2 times. For the imaging experiments, a fluorescence microscope (Olympus Ix50) equipped with an Olympus camera (SC30, Japan) was used to capture the images of cells with CellSens Standard (Olympus Co. Japan) software (Excitation filter: BP530-550, barrier filter: BA590).

Conclusions

We demonstrated a simple one-pot aqueous synthesis approach to generate red-emitting CdTe/CdS/ZnS CSS nanocrystals. Strain-induced optical properties of type-II CdTe/CdS NCs with a very small core and a very thick shell were futher improved with the external growth of a wide bandgap ZnS shell material. The band offsets between CdS and ZnS allowed efficient exciton confinement in the type-II core/shell and, therefore led to increased fluorescence efficiencies (QY_{max} 64 %) and stability. Moreover, cytotoxicity studies proved the reducing effect of an outer ZnS shell by minimizing the destabilization of the NCs. Also, preliminary cell imaging experiments with aptamer-conjugated NCs exhibited effective cell internalization. Remarkably, the aptamer-NC conjugates were stable inside the cells even after 1 day of internalization. In conclusion, the developed CdTe/CdS/ZnS NCs exhibit very high optical efficiencies, stability, as well as reduced toxicity representing an ideal candidate as a fluorescent probe for bio-imaging applications.

Acknowledgements

Notes and references

[a] Gottfried Wilhelm Leibniz University of Hannover, Institute of Technical Chemistry, 30167 Hanover, Germany. E-mail: scheper@iftc.uni-hannover.de

[b] King's College London, Department of Physics, The Strand, WC2R 2LS London, UK. E-mail: mark.a.green@kcl.ac.uk

[c] Hannover Medical School, Biomaterial Engineering, 30625 Hannover, Germany.

† Electronic Supplementary Information (ESI) available: Additional figures for photostability analysis, HRTEM images of different tetrahedral NCs, AFM images of CSS NCs, fluorescence lifetime analysis of CSS NCs and agarose gel electrophoresis of aptamer-NCs conjugates are available. See DOI: 10.1039/b000000x/

RSC Advances Accepted Manuscript

1   A. M. Smith, A. M. Mohs and S. Nie, *Nat Nanotechnol*, 2009, **4**, 56-63.

2   Z. T. Deng, O. Schulz, S. Lin, B. Q. Ding, X. W. Liu, X. X. Wei, R. Ros, H. Yan and Y. Liu, *Journal of the American Chemical Society*, 2010, **132**, 5592-5593.

3   L. N. Chen, J. Wang, W. T. Li and H. Y. Han, *Chem Commun*, 2012, **48**, 4971-4973.

4   P. Reiss, M. Protiere and L. Li, *Small*, 2009, **5**, 154-168.

5   S. Tamang, G. Beaune, I. Texier and P. Reiss, *ACS Nano*, 2011, **5**, 9392-9402.

6   R. G. Xie, M. Rutherford and X. G. Peng, *Journal of the American Chemical Society*, 2009, **131**, 5691-5697.

7   F. Todescato, A. Minotto, R. Signorini, J. J. Jasieniak and R. Bozio, *ACS Nano*, 2013, **7**, 6649-6657.

8   M. Green, P. Williamson, M. Samalova, J. J. Davis, S. Brovelli, P. Dobson and F. Cacialli, *J Mater Chem*, 2009, **19**, 8341-8346.

9   L. L. Li, Y. Chen, Q. Lu, J. Ji, Y. Y. Shen, M. Xu, R. Fei, G. H. Yang, K. Zhang, J. R. Zhang and J. J. Zhu, *Sci Rep-Uk*, 2013, **3**.

10 Z. L. Zhao, L. Xu, X. L. Shi, W. H. Tan, X. H. Fang and D. H. Shangguan, *Analyst*, 2009, **134**, 1808-1814.

11 M. Meyer, T. Scheper and J. G. Walter, *Appl Microbiol Biot*, 2013, **97**, 7097-7109.

12 D. V. Talapin, A. L. Rogach, E. V. Shevchenko, A. Kornowski, M. Haase and H. Weller, *Journal of the American Chemical Society*, 2002, **124**, 5782-5790.

13 M. Lonne, G. H. Zhu, F. Stahl and J. G. Walter, *Biosensors Based on Aptamers and Enzymes*, 2014, **140**, 121-154.

14 J. G. Walter, S. Petersen, F. Stahl, T. Scheper and S. Barcikowski, *J Nanobiotechnology*, **8**, 21.

15 M. Lubbecke, J. G. Walter, F. Stahl and T. Scheper, *Eng Life Sci*, 2012, **12**, 144-151.

16 V. Bagalkot, L. Zhang, E. Levy-Nissenbaum, S. Jon, P. W. Kantoff, R. Langer and O. C. Farokhzad, *Nano Lett*, 2007, **7**, 3065-3070.

17 D. Kim, Y. Y. Jeong and S. Jon, *ACS Nano*, 2010, **4**, 3689-3696.

18 W. J. Kang, J. R. Chae, Y. L. Cho, J. D. Lee and S. Kim, *Small*, 2009, **5**, 2519-2522.

19 H. Shi, X. S. Ye, X. X. He, K. M. Wang, W. S. Cui, D. G. He, D. Li and X. K. Jia, *Nanoscale*, 2014, **6**, 8754-8761.

20 E. V. Shevchenko, D. V. Talapin, H. Schnablegger, A. Kornowski, O. Festin, P. Svedlindh, M. Haase and H. Weller, *Journal of the American Chemical Society*, 2003, **125**, 9090-9101.

21 V. Lesnyak, N. Gaponik and A. Eychmuller, *Chemical Society Reviews*, 2013, **42**, 2905-2929.

22 L. Zou, Z. Y. Gu, N. Zhang, Y. L. Zhang, Z. Fang, W. H. Zhu and X. H. Zhong, *J Mater Chem*, 2008, **18**, 2807-2815.

23 Y. He, H. T. Lu, L. M. Sai, Y. Y. Su, M. Hu, C. H. Fan, W. Huang and L. H. Wang, *Adv Mater*, 2008, **20**, 3416-+.

24 J. N. Tian, R. J. Liu, Y. C. Zhao, Y. Peng, X. Hong, Q. Xu and S. L. Zhao, *Nanotechnology*, 2010, **21**.

25 Z. Li, C. Q. Dong, L. C. Tang, X. Zhu, H. J. Chen and J. C. Ren, *Luminescence*, 2011, **26**, 439-448.

26 S. Taniguchi, M. Green, S. B. Rizvi and A. Seifalian, *J Mater Chem*, 2011, **21**, 2877-2882.

27 Y. Y. Zhang, J. Y. Kim, Y. Kim and D. J. Jang, *J Nanopart Res*, 2012, **14**.

28 W. Jiang, A. Singhal, J. N. Zheng, C. Wang and W. C. W. Chan, *Chem Mater*, 2006, **18**, 4845-4854.

29 M. Bottrill and M. Green, *Chem Commun*, 2011, **47**, 7039-7050.

30 S. J. Soenen, P. Rivera-Gil, J. M. Montenegro, W. J. Parak, S. C. De Smedt and K. Braeckmans, *Nano Today*, 2011, **6**, 446-465.

31 P. Rivera-Gil, D. J. De Aberasturi, V. Wulf, B. Pelaz, P. Del Pino, Y. Y. Zhao, J. M. De La Fuente, I. R. De Larramendi, T. Rojo, X. J. Liang and W. J. Parak, *Accounts Chem Res*, 2013, **46**, 743-749.

32 A. Nel, T. Xia, L. Madler and N. Li, *Science*, 2006, **311**, 622-627.

33 G. X. Liang, L. L. Li, H. Y. Liu, J. R. Zhang, C. Burda and J. J. Zhu, *Chem Commun*, 2010, **46**, 2974-2976.